JOURNAL OF SYNCHROTRON RADIATION
ISSN 1600-5775

Investigation of nanoparticulate silicon as printed layers using scanning electron microscopy, transmission electron microscopy, X-ray absorption spectroscopy and X-ray photoelectron spectroscopy

David M. Unuigbe,[a]* Margit Harting,[b] Emmanuel O. Jonah,[b] David T. Britton[b] and Dennis Nordlund[c]

[a]NanoSciences Innovation Centre, Department of Physics, University of Cape Town, Rondebosch 7701, South Africa, [b]PST Sensors (Pty) Ltd, Cape Town 7405, South Africa, and [c]Stanford Synchrotron Radiation Lightsource, SLAC National Accelerator Laboratory, Menlo Park, CA 94025, USA. *Correspondence e-mail: david.unuigbe@hotmail.com

Received 6 December 2016
Accepted 3 July 2017

Edited by R. W. Strange, University of Essex, UK

Keywords: native oxide; charge transport; sub-oxide states; XANES; XPS; SEM; network structures; printed layers.

The presence of native oxide on the surface of silicon nanoparticles is known to inhibit charge transport on the surfaces. Scanning electron microscopy (SEM) studies reveal that the particles in the printed silicon network have a wide range of sizes and shapes. High-resolution transmission electron microscopy reveals that the particle surfaces have mainly the (111)- and (100)-oriented planes which stabilizes against further oxidation of the particles. X-ray absorption spectroscopy (XANES) and X-ray photoelectron spectroscopy (XPS) measurements at the O 1*s*-edge have been utilized to study the oxidation and local atomic structure of printed layers of silicon nanoparticles which were milled for different times. XANES results reveal the presence of the +4 (SiO_2) oxidation state which tends towards the +2 (SiO) state for higher milling times. Si 2*p* XPS results indicate that the surfaces of the silicon nanoparticles in the printed layers are only partially oxidized and that all three sub-oxide, +1 (Si_2O), +2 (SiO) and +3 (Si_2O_3), states are present. The analysis of the change in the sub-oxide peaks of the silicon nanoparticles shows the dominance of the +4 state only for lower milling times.

1. Introduction

Considerable effort has been made to understand the basic features of the charge transport in systems such as carbon black polymer composites (Zvyagin, 2006), mono-disperse metallic structures (Jonah *et al.*, 2012) and close-packed network systems (Shklovskii & Efros, 1984) such as printed nanoparticulate layers. In printed nanoparticulate silicon systems, surface oxide layers act as insulating layers, which inhibit charge transport. The transport of charge in nanoparticle printed systems can be summarized as hopping percolation charge transport. A main aspect of this understanding was the study of percolation networks using small-angle X-ray scattering (Britton *et al.*, 2009) and ultra-small-angle X-ray scattering (Rai *et al.*, 2012; Jonah *et al.*, 2012) in order to understand the particle size distribution and topology of the particle network, respectively. To further understand the surface topology of a silicon nanoparticle network, a new small-angle scattering technique was developed using beamline 6.3.2 at ALS, Berkeley, USA, employing nanometer-wavelength radiation (Jonah *et al.*, 2014). This structural information of the silicon nanoparticle network has been backed up by electron tomography studies (Jones & Härting, 2013). Electrical characterization of the printed layers shows

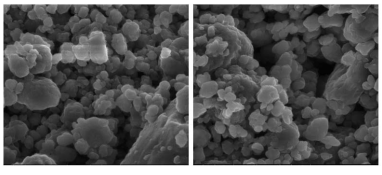

that the charge transport between particles occurs by hopping with different activation energies (Männl *et al.*, 2013). The current study is the first approach using XANES and XPS towards characterizing the oxidation and the local atomic structure of printed silicon nanoparticulate layers.

X-ray absorption near-edge spectroscopy (XANES) and X-ray photoelectron spectroscopy (XPS) are complementary surface analytical techniques widely used in the characterization of materials. They provide information on the local atomic and electronic structure of the absorbing atom due to their sensitivity to the local chemical environment. XANES and XPS are chemically selective techniques that can be used to excite electrons from a particular core level by probing their atoms with an incident X-ray (Bai *et al.*, 2010).

2. Experimental

2.1. Sample preparation

Silicon nanoparticles were produced by high-energy milling of bulk 2503 grade silicon in an 800 W Siebtechnik laboratory orbital disc mill. Nanopowders were milled for periods of 1 h, 2 h, 3 h, 4 h and 5 h. The 2503 grade metallurgical silicon (M-Si) is from silicon smelters, Polokwane, South Africa. Screen printable M-Si inks were produced by adding the powder sequentially into a water-based acrylic emulsion binder supplied by Marchem, Cape Town, South Africa. Each mixture consisted of 75% nanoparticle concentration by weight relative to the binder. To obtain the necessary thixotropic and viscoelastic properties of a screen printed ink (Phair, 2008), propylene glycol supplied by Sigma-Aldrich was used as a thinner to thin the M-Si ink in the mixture.

Test samples were printed using an ATMA AT-60PD semi-automatic flatbed printer on porous 80 gsm plain paper used as substrate. The choice of paper as a substrate in this work was due to its availability and does not matter for the current study. After printing, the samples were left to cure under ambient conditions before measurements were made.

2.2. Scanning electron microscopy

A Nova Nano SEM 230 was utilized to study the morphology of the milled M-Si nanoparticulate printed layers. The printed layers were cut to size and carbon-coated using an evaporation coater. Samples were then mounted on aluminium stubs for surface and cross-sectional viewing. The instrument was operated at a beam energy setting of 5 keV and a current of 200 pA in the secondary electron imaging mode.

2.3. High-resolution transmission electron microscopy

For HRTEM analysis, powdered samples were diluted in ethanol and sonicated for 10 min in order to deaggregate the particles. After sonication, the solution was deposited on holey carbon grids and dried at room temperature. HRTEM images were taken using a FEI TECNAI F20 operating at an alternating voltage of 20 keV with a field emission gun.

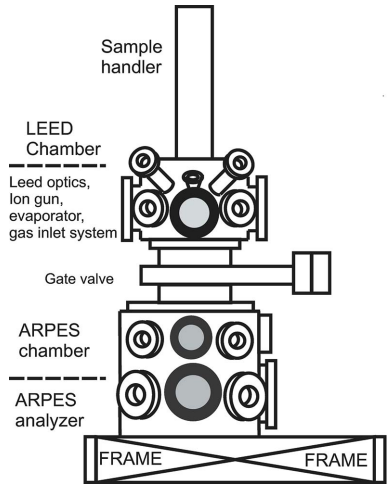

Figure 1
Schematic of the angular-resolved photoelectron spectrometer ARPES (Tobin *et al.*, 1992).

2.4. XANES and XPS

XANES and XPS measurements were carried out at the bending-magnet beamline 8-2 of the Stanford Synchrotron Radiation Laboratory (SSRL). This beamline is operated using a spherical-grating monochromator, has an energy range of 100 eV to 1300 eV, and provides a nominal resolution $\Delta E/E$ of about 4×10^{-4} and a spot size of >0.1 mm. Measurements were performed under UHV conditions after mounting the samples on an aluminium stick using double-sided adhesive carbon tapes. Data were collected using an angular-resolved photoelectron spectrometer (ARPES) equipped with a multichannel detector as shown in Fig. 1. Spectra were recorded in total electron yield (TEY) mode with respect to photon energy by the sample drain current.

3. Results and discussion

3.1. Scanning electron microscopy

Fig. 2 is a micrograph showing a cross-sectional view of the M-Si nanoparticulate printed layer, for the 5 h-milled silicon. Viewing from the top to bottom of the micrograph, the structure that is shown in the image is the paper substrate, nanoparticle printed layer and a tilted view of the top surface. The thickness of the printed layer is estimated to be about twice that of the paper substrate and can be seen to be composed of particles of varying sizes and shapes.

Figs. 3(*a*) and 3(*b*) are SEM micrographs showing the top surface of M-Si nanoparticulate printed layers for 1 h and 5 h milling time. The micrographs are typical pictures at different positions on the surface of the sample. The images show a network of interconnecting particles with shapes that are mostly irregular. The particles are predominantly small with a few large particles and some clusters as seen from the micrographs and demonstrated in the particle size distributions.

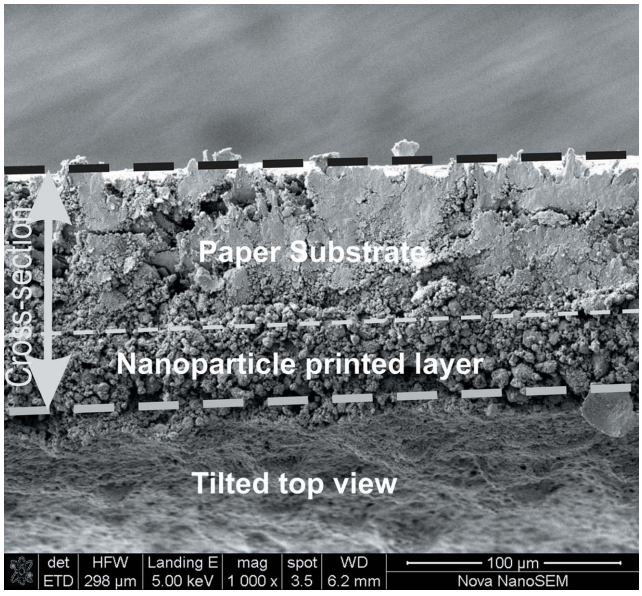

Figure 2
Cross-sectional view of the M-Si nanoparticulate printed layer, 5 h-milled.

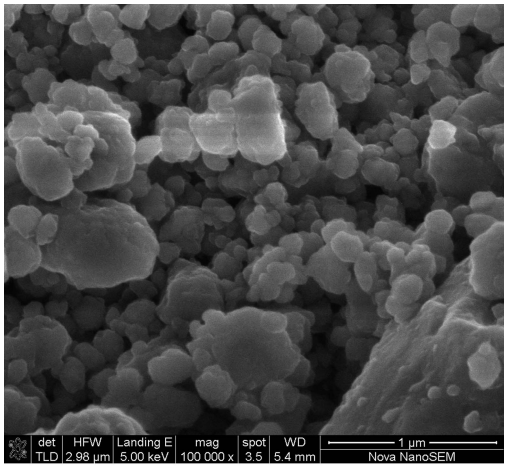

(*a*)

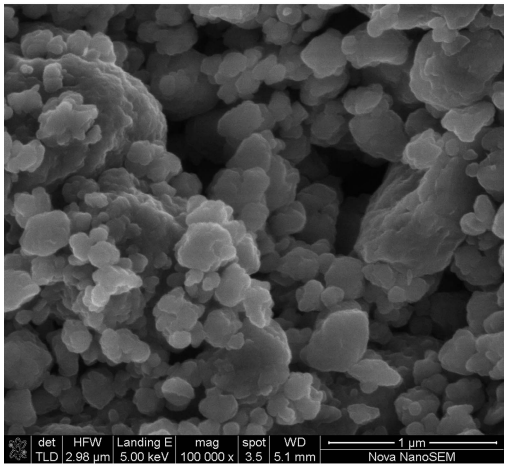

(*b*)

Figure 3
(*a*) Micrograph of the M-Si nanoparticulate printed layer, 1 h-milled. (*b*) Micrograph of the M-Si nanoparticulate printed layer, 5 h-milled.

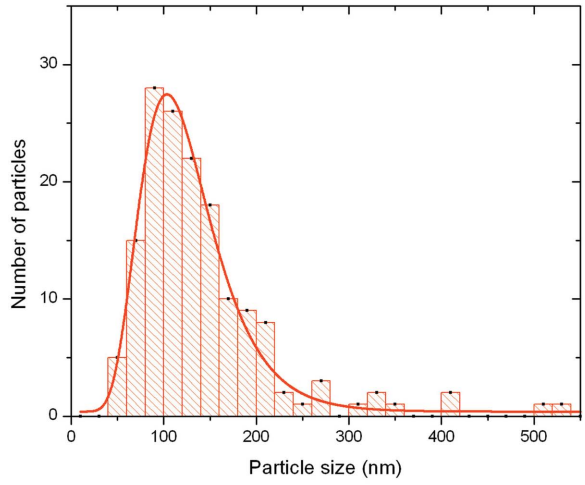

(*a*)

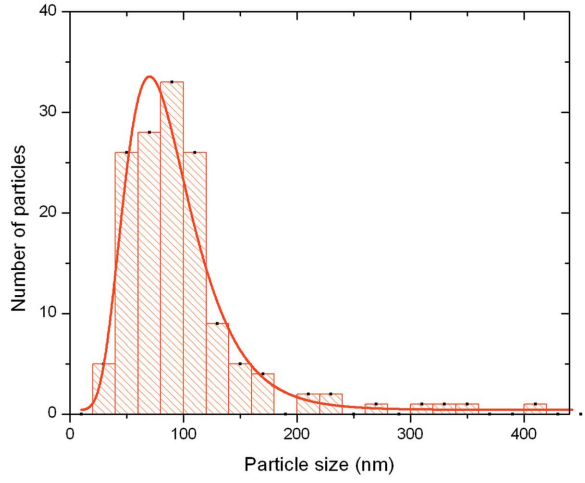

(*b*)

Figure 4
(*a*) Particle size distribution of the M-Si nanoparticulate printed layer, 1 h-milled. (*b*) Particle size distribution of the M-Si nanoparticulate printed layer, 5 h-milled.

Figs. 4(*a*) and 4(*b*) show the particle size distributions of the 1–5 h M-Si nanoparticulate printed layers. The mean particle sizes were determined after fitting the particle size distributions with a lognormal distribution.

The variation of the particle size with milling time is presented in Fig. 5. This demonstrates that the mean particle size in the M-Si nanoparticulate printed layers decreases with the nanoparticle milling time.

3.2. High-resolution transmission electron microscopy

HRTEM images of 5 h-, 3 h- and 1 h-milled silicon particles are presented in Figs. 6(*a*)–6(*f*). The micrographs were taken seven months after the powders were milled by drop casting into holey carbon grids.

The morphology of the particles as shown in Figs. 6(*a*)–6(*c*) is similar to those revealed by SEM with mostly irregularly shaped particles and some clusters. Figs. 6(*d*)–6(*f*) reveal that there is no evidence of amorphization. Structural analysis of silicon nanoparticles produced by ball milling shows that the

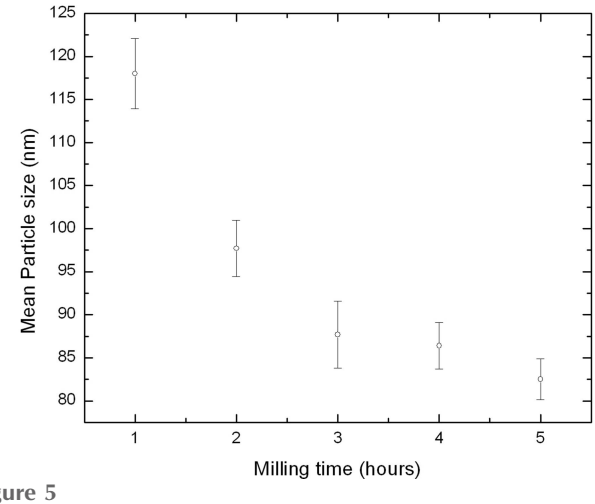

Figure 5
Variation of the mean particle size with milling time.

lattice undergoes transformations and, although the structure is mostly crystalline, amorphous phases are present (Svrcek *et al.*, 2005; Gaffet & Harmelin, 1990; Unifantowicz *et al.*, 2007).

The facets as observed in Figs. 6(*d*) and 6(*e*) have mainly the (111)- and (100)-oriented surfaces as indicated by their lattice planes with a few (110) surfaces, which can be seen in Fig. 6(*f*). The internal form of the particles is polycrystalline with a particle grain size within the range 10–20 nm with few dislocations present. The lattice planes can be traced down to the surface of the particles as seen in the micrographs indicating that the surface is not disordered.

3.3. XANES and XPS

In order to characterize the oxidation and local atomic structure of the printed nanoparticulate layers, O 1*s*-edge XANES was carried out within the range –50 eV to +50 eV with respect to the absorption-edge position.

Fig. 7(*a*) shows the O 1*s* XANES spectra of the 1 h to 5 h M-Si milled nanoparticles as printed layers. In all spectra, background reduction and edge step normalization was carried out with the package *ATHENA* which uses the Autobackup algorithm (Ravel & Newville, 2005). The data reduction procedure corrects for possible self-absorption effects, removal of the pre-edge background, and the normalization to unity. The background continuum was removed using an arctangent function (Stebbins & Xue, 2014).

In our spectra, the absorption edge, which is the rise in the absorption, μ, by core O 1*s* electrons due to absorption of photons, starts at about 532 eV. The spectra have strong structure to at least 30 eV above the threshold. Peaks identified in all spectra are the pre-edge peak at 533 eV (peak I), π resonance peak at 538 eV (peak II) and a post-edge peak at about 20 to 30 eV (peak III) above the absorption edge. The pre-edge peak is assigned to the oxygen 2*p* to transition metal 3*d* hybridization (De Groot *et al.*, 1989) and is suggestive of a decrease in band gap by the presence of impurities (Green *et al.*, 2014). The origin of this impurity has not been investigated in this report but is likely to be an impurity from the feedstock material or to have been introduced during the production of the silicon nanoparticulate powders. The specified purity of the bulk silicon from the suppliers was 99.4%.

The π resonance peak in the region ~538–540 eV arises from the SiO_2 tetrahedral bonding and is assigned to the SiO_x tetrahedral structure. It corresponds to the transition from the oxygen 1*s* to 2*p* and Si 3*s* and 3*p* hybrid states (Lin *et al.*, 2007).

The resonance peak at ~560 eV can be attributed to the Si–Si second neighbour distance related to the Si—O—Si bond angle (Lagarde *et al.*, 1992). It arises from the oxygen 2*p* hybrid states with silicon *d* molecular orbitals and is generally referred to as the σ resonance peak (Wu *et al.*, 1998; Baba *et al.*, 1993).

In order to obtain quantitative information from the XANES data, the spectra in Fig. 7(*a*) were fit with a suitable background function (a sigmoidal function), and two Gaussian functions for the π and σ resonance peaks. In the fitting procedure, the intensity of the σ peak height was set to a constant value since all our spectra were normalized to the peak height of the σ peak. However, the intensity of the π resonance peak was left to vary. The relative intensities obtained from the fit results in our spectra are presented in Fig. 7(*b*).

It can be noticed from Fig. 7(*b*) that there is a gradual decrease in the relative π to σ resonance peak relative peak intensities with increasing nanoparticle milling time. This trend is suggestive of oxide reduction during the production

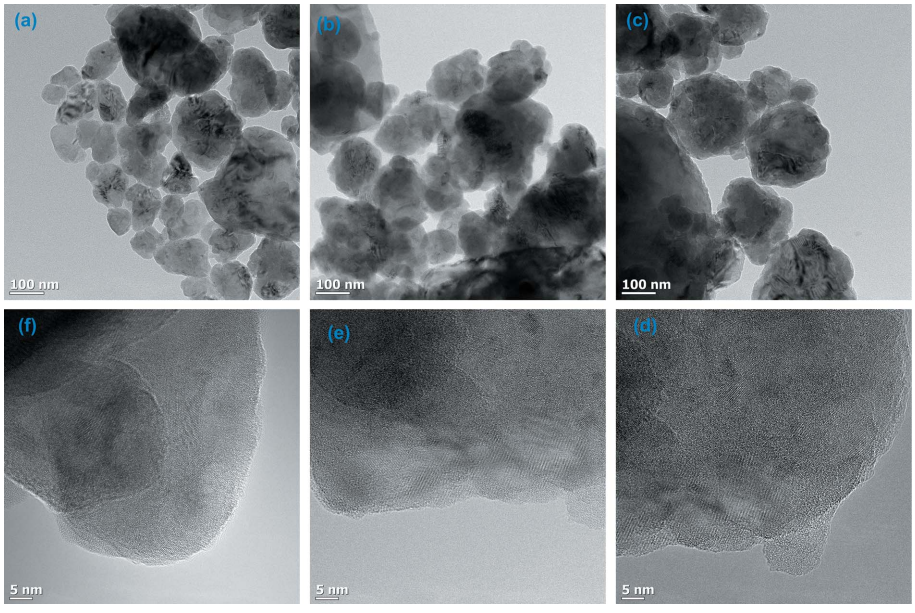

Figure 6
HRTEM images showing (*a*, *b*, *c*) the internal structure of the particles for 5 h-, 3 h-, 1 h-milled particles, and (*d*, *e*, *f*) the particle surfaces for 5 h, 3 h and 1 h milling, respectively.

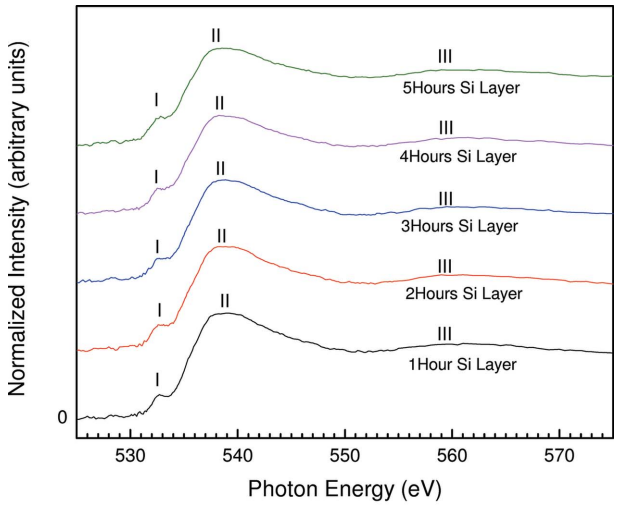

(*a*)

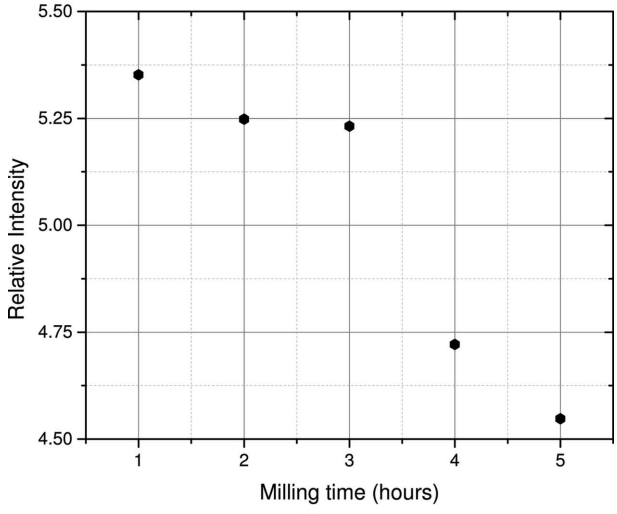

(*b*)

Figure 7
(*a*) Normalized O 1*s*-edge XANES plot of printed nanoparticulate silicon layers on paper substrate (metallurgical silicon milled for 1–5 h). (*b*) Relative intensity of the π to σ resonance peak of printed nanoparticulate silicon layers with respect to nanoparticle milling time.

of the nanoparticles by milling. Furthermore, the structure of the SiO_4 microscopic unit state changes with increasing milling time with less oxide bonded to the silicon.

In order to obtain further insight on the oxidation and local structure of our materials, high-resolution XPS measurements have been used to characterize our milled silicon nanoparticle printed layers. The XPS technique is based on the principle of the photoelectric effect, which was introduced by Einstein. The relationship for the photoelectric effect between an incident X-ray photon ($h\upsilon$) and atoms of a material, leading to the ejection of photoelectrons with kinetic energy (KE), is given as

$$\mathrm{KE} = h\upsilon - \mathrm{BE} - \varphi, \qquad (1)$$

where BE is the binding energy of the electrons in the atom and φ is the work function of the spectrometer (Koningsberger & Prins, 1988).

For the purpose of high-resolution XPS analysis, an excitation energy of 650 eV was utilized. Figs. 8(*a*) and 8(*b*) show the fitted Si 2*p* XPS spectra for the 1 h- to 5 h-milled silicon nanoparticulate printed layers. The peaks at ∼99.8 eV and ∼103.8 eV correspond to an atom of elemental silicon (with no oxygen bond) and a silicon–oxygen tetrahedron, respectively. Si^{1+}, Si^{2+} and Si^{3+} correspond to silicon bonded by one, two and three oxygen atoms, respectively (Jolly *et al.*, 2001).

In our spectra, background subtraction was carried out by fitting a Shirley function to the data. Spectra were fitted with a superposition of five Gaussian functions corresponding to the different oxidation states of Si. The relative concentrations of the oxidation states were determined using the ratio $I_{\mathrm{Si}^{n+}}/I_{\mathrm{total}}$ (n = 0, 1, 2, 3 and 4) (Bianconi, 1988).

From the high-resolution Si 2*p* XPS scans shown in Figs. 8(*a*) and 8(*b*), the two main peaks observed correspond to elemental silicon Si^0 at 99.8 eV binding energy and fully oxidized silicon state Si^{4+} at 103.8 eV. The spectrum also shows photoemission, where an intermediate sub-oxide state can be

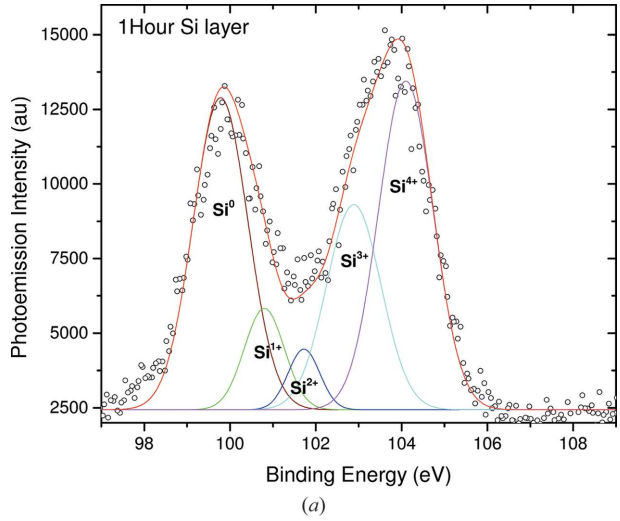

(*a*)

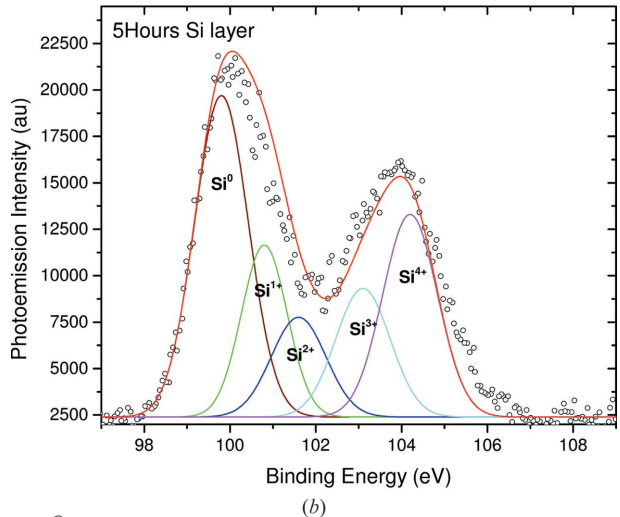

(*b*)

Figure 8
(*a*) Si 2*p* XPS spectrum of the M-Si nanoparticulate printed layer, 1 h-milled. (*b*) Si 2*p* XPS spectrum of the M-Si nanoparticulate printed layer, 5 h-milled.

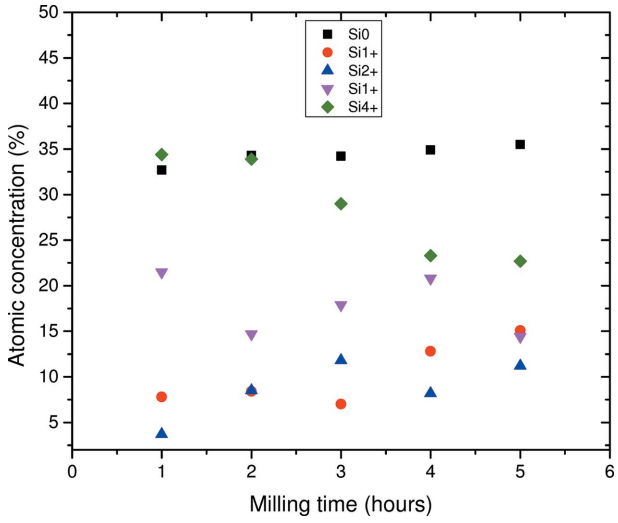

Figure 9
Variation in concentration of the five Si sub-oxide states with milling time.

resolved, from other bonded oxygen configurations in addition to the elemental and fully oxidized states.

Fig. 9 shows the changes in concentration of the five sub-oxide states as a function of nanoparticle milling time. For lower milling times, the dominant state in the printed nanoparticulate silicon layers was the Si^{4+} state whereas the Si^{0} state appears more prominently for higher milling times in the layers. The concentrations of the Si^{4+} state decreased while that of the Si^{0} state increased with nanoparticle milling time. As the nanoparticle milling time increases, the concentration of Si^{1+} and Si^{2+} sub-oxide states tends to increase whereas the Si^{3+} state shows no particular trend. The dominance of the Si^{0} sub-oxide state at higher nanoparticle milling time indicates fewer oxygen bonded to the silicon nanoparticles. The silicon structure changes from that of the SiO_4 microstructure (+4 state) to a lower Si sub-oxide state. The long-term stability of the silicon particles after production against atmospheric oxygen and in aqueous environment is of importance. We have been able to show that, for these particles produced by high-energy milling, although the particle surface is not completely free of oxygen, the particles are not fully oxidized. The formation of an insulating oxide layer is inhibited by the chemical passivation of the silicon surface with oxygen. The passivation layer is enabled by the dominance of the (111)- and (100)-oriented surfaces on the polycrystalline nanoparticles which is in line with established models for the initial oxidation of silicon (Chabal *et al.*, 2002; Hemeryck *et al.*, 2007).

4. Conclusions

Scanning electron microscopy studies of the nanoparticulate printed layers show an interconnecting network of particles with irregular shapes and varying sizes. The mean sizes of the particles in the network structure reduce with the nanoparticle milling time. High-resolution transmission electron microscopy shows that the particles are irregularly shaped and are polycrystalline. The particle surfaces are predominantly the (111) and (100) facets which results in the passivation of the silicon surface with oxygen.

X-ray absorption spectroscopy and X-ray photoelectron spectroscopy reveal the evolution of the oxidation in printed nanoparticulate silicon layers on paper substrate for different nanoparticle milling times. XANES reveals the structure changes from the SiO_4 microstructure to a silicon atom with fewer oxygen bonded to the silicon. At lower nanoparticle milling times, the Si^{4+} sub-oxide state is dominant and gradually reduces with increasing nanoparticle milling time.

Acknowledgements

This work was supported in part by the NanoPower Africa Project funded by United States Agency for International Development (USAID) through the Higher Education for Development (HED) office. Additional funding to the UCT NanoSciences Innovation centre was provided by the US Airforce Office of Scientific Research through the project 'Nanoparticle Solutions for Printed Electronic Applications', by the University of Cape Town Vice Chancellor's Strategic Fund, and by the South African National Research Foundation (NRF) under focus area grant FA20064160004. The development of the printed silicon materials was supported by DST through its business unit the Technology Innovation Agency under Technology Advancement Project T50055.

References

Baba, Y. H., Yamamoto, H. & Sasaki, T. A. (1993). *Phys. Rev. B*, **48**, 10972–10977.
Bai, Y., Liu, X., Cook, P., Abbott, N. L. & Himpsel, F. J. (2010). *Langmuir*, **26**, 6464–6470.
Bianconi, A. (1988). *X-ray Absorption: Principles, Applicatioons, Techniques of EXAFS, SEXAFS and XANES*, edited by D. C. Koningsberger & R. Prins, pp. 573–66. New York: Wiley Interscience.
Britton, D. T., Odo, E. A., Gonfa, G. G., Jonah, E. O. & Härting, M. (2009). *J. Appl. Cryst.* **42**, 448–456.
Chabal, Y. J., Raghavachari, K., Zhang, X. & Garfunkel, E. (2002). *Phys. Rev. B*, **66**, 161315.
Gaffet, E. & Harmelin, M. (1990). *J. Less-Common Metals*, **157**, 201–222.
Green, R. J., Zatsepin, D. A., Onge, D. J. St., Kurmaev, E. Z., Gavrilov, N. V., Zatsepin, A. F. & Moewes, A. (2014). *J. Appl. Phys.* **115**, 103708.
Groot, F. M. F. de, Grioni, M., Fuggle, J. C., Ghijsen, J., Sawatzky, G. A. & Petersen, H. (1989). *Phys. Rev. B*, **40**, 5715–5723.
Hemeryck, A., Mayne, A. J., Richard, N., Estève, A., Chabal, Y. J., Djafari Rouhani, M., Dujardin, G. & Comtet, G. (2007). *J. Chem. Phys.* **126**, 114707.
Jolly, F., Rochet, F., Dufour, G., Grupp, C. & Taleb-Ibrahimi, A. (2001). *J. Non-Cryst. Solids*, **280**, 150–155.
Jonah, E. O., Britton, D. T., Beaucage, P., Rai, D. K., Beaucage, G., Magunje, B., Ilavsky, J., Scriba, M. R. & Härting, M. R. (2012). *J. Nanopart. Res.* **14**, 1249.
Jonah, E. O., Härting, M., Gullikson, E., Aquila, A. & Britton, D. T. (2014). *J. Synchrotron Rad.* **21**, 547–553.
Jones, S. D. & Härting, M. (2013). *Ultramicroscopy*, **135**, 56–63.
Koningsberger, D. C. & Prins, R. (1988). *X-ray Absorption: Principles, Applications, Techniques of EXAFS, SEXAFS, and XANES*. New York: Wiley.

Lagarde, P., Flank, A., Tourillon, G., Liebermann, R. & Itie, J. (1992). *J. Phys. I*, **2**, 1043–1050.
Lin, J. F., Fukui, H., Prendergast, D., Okuchi, T., Cai, Y. Q., Hiraoka, N., Yoo, C., Trave, A., Eng, P., Hu, M. Y. & Chow, P. (2007). *Phys. Rev. B*, **75**, 012201.
Männl, U., Chuvilin, A., Magunje, B., Jonah, E. O., Härting, M. & Britton, D. T. (2013). *Jpn. J. Appl. Phys.* **52**, 05DA11.
Phair, J. W. (2008). *J. Am. Ceram. Soc.* **91**, 2130–2137.
Rai, D. K., Beaucage, G., Jonah, E. O., Britton, D. T., Sukumaran, S., Chopra, S., Gonfa, G. G. & Härting, M. (2012). *J. Chem. Phys.* **137**, 044311.
Ravel, B. & Newville, M. (2005). *J. Synchrotron Rad.* **12**, 537–541.
Shklovskii, B. I. & Efros, A. L. (1984). *Electronic Properties of Doped Semiconductors*, Vol. 45 of *Springer Series in Solid-State Sciences*. Berlin/Heidelberg: Springer.
Stebbins, J. F. & Xue, X. Y. (2014). *Spectroscopic Methods in Mineralogy and Material Sciences*, Vol. 78 of *Reviews in Mineralogy and Geochemistry*, edited by G. S. Henderson, D. R. Neuville and R. T. Downs, ch. 15, pp. 605–653. Mineralogical Society of America.
Svrcek, V., Rehspringer, J., Gaffet, E. & Muller, J. C. (2005). *J. Cryst. Growth*, **276**, 589–597.
Tobin, J. G., Waddill, G. D., Li, H. & Tong, S. Y. (1992). *MRS Proc.* **295**, 213.
Unifantowicz, P., Vaucher, S., Lewandowska, M. & Kurzydlowski, K. J. (2007). *J. Phys. Condens. Matter*, **20**, 025205.
Wu, Z. Y., Jollet, F. & Seifert, F. (1998). *J. Phys. Condens. Matter*, **10**, 8083.
Zvyagin, I. (2006). In *Charge Transport in Disordered Materials with Applications in Electronics*, edited by S. Baranovski. John Wiley and Sons Ltd.